


Periodic-Phase Acoustic Vortices with Tunable Comblike Orbital Angular Momentum Spectrum

Xin-Rui Li¹, Jia-Jia Feng¹, Bu-Chen Ping¹, Yang Sun¹, Da-Jian Wu^{1,*} and Badreddine Assouar^{2,†}

¹*Jiangsu Key Lab of Opto-Electronic Technology, School of Physics and Technology, Nanjing Normal University, Nanjing 210023, China*

²*Université de Lorraine, CNRS, Institut Jean Lamour, Nancy 54000, France*

 (Received 8 May 2023; revised 6 June 2023; accepted 23 August 2023; published 6 September 2023)

Acoustic vortices (AVs) carrying orbital angular momentum (OAM) have shown great significance in communication. However, crosstalk in acoustic communication based on traditional AVs with single OAM remains an issue. Here, we propose a periodic-phase acoustic vortex (PPAV) with a comblike OAM spectrum. The sample interval of the OAM spectrum of the PPAV can be modulated by the period number of the azimuthal phase. The influence of the period number on the acoustic properties of the PPAV and the evolution of the PPAV are investigated theoretically. Moreover, an acoustic artificial-structure plate engraved with 24 filled circular holes is designed to generate the PPAV in water. By changing the height of the resin layer filling each hole unit, the transmitted phase shift of the ultrasonic wave through them can be flexibly and efficiently manipulated. Both simulations and experiments confirm that the designed artificial plate with filled holes can produce the PPAV with an arbitrary topological charge. Finally, we preliminarily explore the possibility of applying the PPAV in acoustic communication and show that the OAM sample interval of the PPAV can be used as an independent degree of freedom for acoustic encoding-decoding communication. We believe that the PPAV generated by the acoustic artificial-structure plates may find good applications in microparticle manipulation and acoustic communication.

DOI: [10.1103/PhysRevApplied.20.034008](https://doi.org/10.1103/PhysRevApplied.20.034008)

I. INTRODUCTION

Orbital angular momentum (OAM), one of the basic physical natures of an acoustic vortex (AV), has gained increasing interest due to its applications in microparticle manipulation and acoustic communication [1–9]. Theoretically, the communication capacity of the OAM beam can be increased infinitely due to the orthogonality of OAMs with different modes [10–13]. Accordingly, a series of investigations concentrated on OAM multiplexing and demultiplexing in acoustic communication, which was demonstrated to be able to greatly increase the information capacity. In communication, crosstalk is a crucial problem that causes disruptions within the process of data transmission and it is inevitable [14–16]. The crosstalk between orthogonal bases is an important index to verify the accuracy and robustness of an acoustic communication system, and greater crosstalk between orthogonal bases will result in a degradation of the signals that are received [4,17]. Therefore, it is highly desirable to construct acoustic communications with minimal channel crosstalk [18]. Conventional integer AVs have a single OAM that is merely

determined by the topological charge (TC) [14,19]. Many investigations have shown that the energy of a transmitted single OAM mode will be leaked into the neighboring OAM modes and other channels [16,20,21], and hence, the expected information at the receiver end does not match with the measured transmitted modes [15]. Recently, it was reported that the optical vortex (OV), carrying more OAM modes, was beneficial for reducing mode crosstalk [22,23] and increasing robustness [24]. Accordingly, many OVs with more OAM modes and tailorable OAM spectra have been proposed and investigated [25–29]. In this context, OAM multiformity of the AV could also help to improve the communication quality.

Ultrasonic waves are dominant carriers of underwater communication because of the rapid decay of light and electromagnetic waves [2,14,30] in such a medium. Acoustic artificial metamaterials have received a lot of attention recently in ultrasonic research [31–33], opening up an alternative path for the manipulation of ultrasonic waves. Furthermore, considerable efforts have been devoted to investigations on the generation of ultrasonic AVs and their underwater applications, especially in acoustic communications [2,3,34,35]. The general method for generating the ultrasonic AV is based on a transducer array that can flexibly modulate the generation of the ultrasonic

*wudajian@njnu.edu.cn

†badreddine.assouar@univ-lorraine.fr

AV [3]. A passive method based on the artificial-structure plate is another choice, and it has attracted great attention due to its advantages of simplicity, economy, and ease of miniaturization. Many strategies, such as multiarm coiling slits, discrete spiral structure plates, and degenerate pinhole plates, have been successfully explored to realize ultrasonic AVs in water; these have found further applications in microparticle manipulation and acoustic communication. However, for an ultrasonic AV with a large TC or the multimode ultrasonic AV, single-spatial-phase modulation cannot meet the designed phase requirements. Hence, an additional regulatory degree of freedom is needed.

Here, we propose a periodic-phase acoustic vortex (PPAV) with a comblike OAM spectrum. By changing the period number of the azimuthal phase, the sample interval of the OAM spectrum of the PPAV can be adjusted. The normalized acoustic intensity distributions, phase distributions, and OAM spectra of the PPAV are carefully studied through theoretical analysis and numerical simulation. An acoustic artificial-structure plate (AASP) engraved with 24 filled circular holes (CHs) is designed to achieve the PPAVs in water. By changing the height of the resin layer filling each hole unit, the transmitted phase shift of the ultrasonic wave through them can be flexibly and efficiently manipulated. Hence, PPAVs with arbitrary TCs and OAM sample intervals can be achieved. Further experiments confirm that the proposed AASP can generate the PPAV. Finally, we illustrate the possibility of acoustic encoding-decoding communication based on the OAM sample interval of the PPAV.

II. THEORETICAL ANALYSIS

To better introduce the proposed concept of the PPAV, we start from the definition of the conventional acoustic vortex (CAV). The acoustic field of CAV can be expressed as [4]

$$P_{\text{CAV}}(r, \theta) = P_0 \exp(i\psi_{\text{CAV}}), \quad (1)$$

where P_0 is the amplitude, the phase of the CAV is $\psi_{\text{CAV}} = m\theta$, m means the TC, and azimuthal angle θ increases from 0 to 2π . Similar to the CAV [4], the acoustic field of the proposed PPAV can be written as

$$P_{\text{PPAV}}(r, \theta) = P_0 \exp(i\psi_{\text{PPAV}}), \quad (2)$$

where P_0 and ψ_{PPAV} are the amplitude and phase of the PPAV, respectively. The phase of the PPAV, ψ_{PPAV} , is divided into N periods as azimuthal angle θ increases from 0 to 2π . The phase shift in each period is $2\pi l/N$, where l is the TC of the PPAV. Each period consists of two piecewise phase functions, the first of which has a phase shift that is an integral multiple of 2π ($A = 2\pi n$) and the second of which has a fractional phase jump ($B = 2\pi l/N - 2\pi n$), where $n = [l/N]$ is the phase-jump factor and $[.]$ denotes the lowest-integer function. Therefore, the phase function of the PPAV in the first period is expressed as

$$\psi_{\text{PPAV}} = \begin{cases} l\theta, & 0 \leq \theta < \frac{2\pi n}{l}, \\ l\theta - 2\pi n, & \frac{2\pi n}{l} \leq \theta < \frac{2\pi}{N}. \end{cases} \quad (3)$$

Then, as azimuthal angle θ increases from 0 to 2π , the phase function of the PPAV can be written as

$$\psi_{\text{PPAV}} = \begin{cases} l\left(\theta - \frac{2\pi q}{N}\right), & \frac{2\pi q}{N} \leq \theta < \frac{2\pi n}{l} + \frac{2\pi q}{N}, \\ l\left(\theta - \frac{2\pi q}{N}\right) - 2\pi n, & \frac{2\pi n}{l} + \frac{2\pi q}{N} \leq \theta < \frac{2\pi(1+q)}{N} \end{cases} \quad (q = 0, 1, \dots, N-1). \quad (4)$$

The acoustic field of the PPAV can be expressed as

$$P_{\text{PPAV}}(r, \theta) = \sum_{q=0}^{N-1} p\left(r, \theta + \frac{2\pi q}{N}\right), \quad (5)$$

where $p(r, \theta)$ denotes the acoustic field of each azimuthal phase period. It was reported that an arbitrary acoustic field could be decomposed into a set of orthonormal bases, such as integer OAM states [36]. Therefore, $p(r, \theta)$ can be rewritten as [27,28]

$$p(r, \theta) = P_0 \sum_{L=-\infty}^{\infty} c_L \exp(iL\theta), \quad (6)$$

where $c_L = \langle \exp(iL\theta) | \exp(i\psi_{\text{PPAV}}) \rangle$ represents the expansion coefficient.

Substituting Eq. (6) into Eq. (5), we obtain

$$P_{\text{PPAV}}(r, \theta) = P_0 \sum_{L=-\infty}^{\infty} \sum_{q=0}^{N-1} c_L \exp\left[iL\left(\theta + \frac{2\pi q}{N}\right)\right]. \quad (7)$$

The summation over q can be expressed as [36]

$$\sum_{q=0}^{N-1} \exp\left(iL\frac{2\pi q}{N}\right) = \begin{cases} N, & L = KN, \\ 0, & L \neq KN, \end{cases} \quad (8)$$

where K is an integer. Then, Eq. (7) can be rewritten as

$$P_{\text{PPAV}}(r, \theta) = \begin{cases} P_0 N \sum_{L=-\infty}^{\infty} c_L \exp(iL\theta), & L = KN, \\ 0, & L \neq KN. \end{cases} \quad (9)$$

Therefore, the proposed PPAV has a comblike OAM spectrum with a sample interval of N .

III. ANALYTICAL RESULTS AND DISCUSSION

To realize the PPAVs, we first design a theoretical model in which 24 acoustic sources are evenly assigned on a circle with a radius of r to generate the desired initial phase. Figure 1(a) shows a schematic diagram of the original analytical model for generating a PPAV with $l=3$ and $N=2$, where 24 acoustic sources are evenly placed on a circle with a radius of r . The location of the j th acoustic source is defined as $(r, \theta_j, 0)$, where $\theta_j = 2\pi(j-1)/24$ and its corresponding phase ψ_j can be calculated using Eq. (4). According to Refs. [8,37], the acoustic field generated by these acoustic sources can be written as

$$P(\rho, \varphi, z, t) = \exp(-i\omega t) \sum_{j=1}^{24} \frac{P_0}{R_j} \exp(ikR_j) \exp(i\psi_j), \quad (10)$$

where $R_j = \sqrt{(\rho \cos \varphi - r \cos \theta_j)^2 + (\rho \sin \varphi - r \sin \theta_j)^2 + z^2}$ is the distance from the j th acoustic source $(r, \theta_j, 0)$ to the observation point (ρ, φ, z) [8,37].

Throughout this work, the background medium is water, the incident frequency is fixed at 1 MHz, and the circle radius r is set as 14λ . Figure 1(b) shows the dependence of the phase, ψ_{PPAV} , of the PPAV with $l=3$ and $N=2$ on θ . There are two phase periods, and each period provides a phase shift of $[(3 \times 2\pi)/2 = 3\pi]$. As azimuthal angle θ increases from 0 to $2\pi/3$, ψ_{PPAV} increases from 0 to 2π , and hence, $A = 2\pi$. As θ further increases from $2\pi/3$ to π , ψ_{PPAV} increases from 0 to π , and thus, $B = \pi$. In the second period of $(\pi \leq \theta \leq 2\pi)$, the same variation of ψ_{PPAV} is observed with $A = 2\pi$ and $B = \pi$. Figure 1(c) shows the normalized analytical acoustic intensity distribution of the PPAV with $l=3$ and $N=2$ at a plane of $z = 7\lambda$. It should be noted that 7λ is not the limiting propagation distance of the PPAVs. In the Supplemental Material [42], we further examine the propagation characteristics of the PPAV. It is noted that the PPAV can reach a considerable distance. There is a bright spot on the positive y axis, while a dark one (indicated by a white open circles) can be observed between the origin of coordinates and the bright spot. Symmetrically, another dark spot and a bright spot that can be found along the negative y axis. Meanwhile, two bright fringes can be found on the x axis, while two dark stripes (indicated by two red-dashed ellipses) between the origin

and the bright fringes appear symmetrically on the positive and negative x axis, respectively. The corresponding phase distribution is shown in Fig. 1(d), where two phase singularities (indicated by two white open circles) on the y axis correspond to the two dark spots and two phase singularities (represented by red-dashed ellipses) on the x axis correspond to two dark stripes. In the Supplemental Material [42], we further study the acoustic intensity and phase distributions produced by the first and second phase periods of the PPAV, with $l=3$ and $N=2$, and confirm that a fractional phase jump of π in the first and second phase periods can make the central phase singularity split along the y axis, resulting in two phase singularities on the positive and negative y axis. Moreover, the coupling between two phase periods induces phase-singularity splitting along the x axis, resulting in two phase singularities on the positive and negative x axis. Figure 1(e) shows the OAM spectrum of the PPAV with $l=3$ and $N=2$. According to Eqs. (8) and (9), the superposition of OAM states is only nonvanishing when OAM component L is equal to KN . Therefore, the sample interval of the components in the OAM spectrum of the PPAV with $l=3$ and $N=2$ is 2. The power is mainly distributed in two OAM components of $L=2$ and 4, and the power weights of both are about 43.8%. In addition, there are some weak OAM modes that can be observed in Fig. 1(e). The power weights of OAM components of $L=0, 6, 8,$ and 10 are about 4.87%, 4.87%, 1.7%, and 0.9%, respectively, which are in accordance with the weak acoustic fields distributed at the center and the edges.

Next, we investigate the evolution of the PPAV with TC increasing from 2 to 4 when the period number, N , is fixed at 2. In Fig. 2, the first row shows the dependency of the phase, ψ_{PPAV} , of the PPAVs with TCs $l=2, 2.5, 3, 3.5,$ and 4 on θ . For $N=2$, the phase shifts are $A=2\pi$ for the PPAVs with $l=2, 2.5, 3,$ and 3.5 , and the corresponding fractional phase jumps are $B=0, 0.5\pi, \pi,$ and 1.5π , respectively. For the PPAV with $l=4$, the phase shift, A , is 4π and the phase jump, B , is 0. The second row shows the normalized analytical acoustic intensity distributions of the PPAVs with $l=2$ [Fig. 2(b1)], 2.5 [Fig. 2(b2)], 3 [Fig. 2(b3)], 3.5 [Fig. 2(b4)], and 4 [Fig. 2(b5)] at a plane of $z = 7\lambda$, while the corresponding phase distributions of the PPAVs are shown in Figs. 2(c1)–2(c5). The bottom row shows the OAM spectra of the PPAVs with $l=2$ [Fig. 2(d1)], 2.5 [Fig. 2(d2)], 3 [Fig. 2(d3)], 3.5 [Fig. 2(d4)], and 4 [Fig. 2(d5)]. When $l=2$ ($A=2\pi$ and $B=0$), the PPAV returns to the CAV. The normalized analytical acoustic intensity distribution of the PPAV is ringlike, while the phase changes by 4π along the anti-clockwise direction. Moreover, the power weight of the OAM component of $L=2$ is about 100%, as shown in Fig. 2(d1). These characteristics are consistent with those of the CAV with a TC of 2. As l increases to 2.5, the fractional phase jump, B , increases from 0 to 0.5π . The

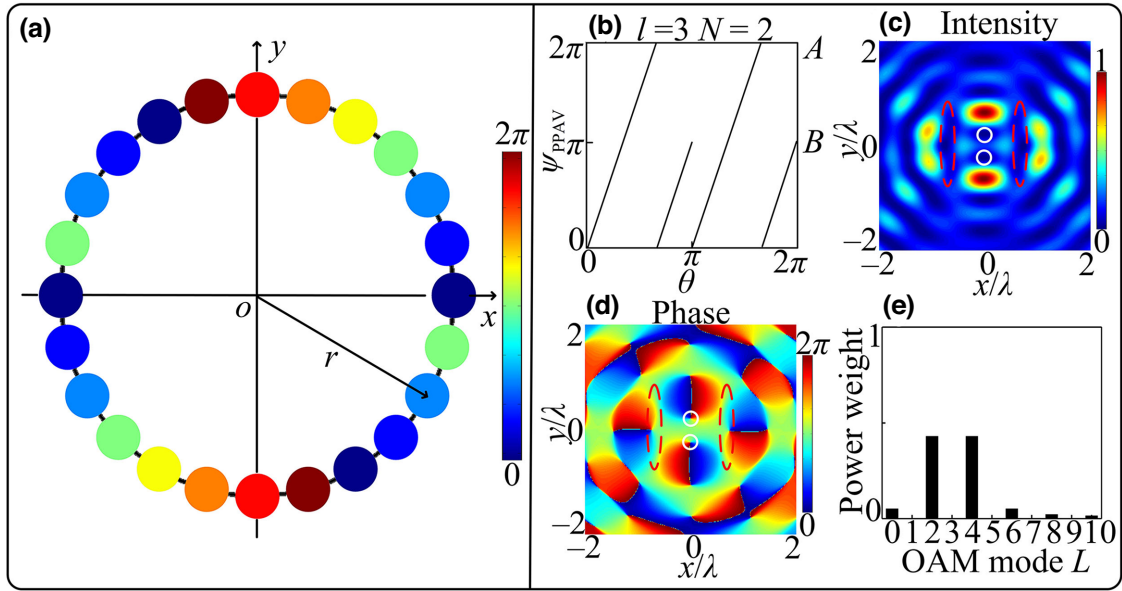


FIG. 1. (a) Schematic diagram of an original analytical model for a PPAV with TC $l=3$ and period number $N=2$. (b) Dependence of the phase, ψ_{PPAV} , of the PPAV with $l=3$ and $N=2$ on azimuthal angle θ . (c) Normalized analytical acoustic intensity and (d) phase distributions of the PPAV with $l=3$ and $N=2$. (e) Corresponding OAM spectrum of the PPAV.

central phase singularity splits along the y axis, and hence, the inner ringlike intensity pattern is broken [37], and two phase singularities on the positive and negative x axis gradually take shape. In this case, the power weight of the OAM component of $L=2$ decreases to about 84.5%. According to Eq. (9), there are still some other components in the OAM spectrum with a sample interval of two. The power weight of the OAM components of $L=0, 4, 6, 8$, and 10 are about 3.4%, 9%, 1.7%, 0.69%, and 0.36%, respectively. As l increases to 3, the fractional phase jump, B , increases to π and the splitting of the phase singularity becomes maximum. The offset of two phase singularities on the positive and negative y axis reaches a maximum, and two phase singularities on the positive and negative x axis are fully formed. There is a bright spot on the positive y axis, while a dark one can be observed between the origin of the coordinates and the bright spot. Symmetrically, another dark spot and a bright spot can be found along the negative y axis. Two bright fringes on the x axis are obvious, while two dark stripes between the origin of the coordinates and the bright fringes are fully generated. Correspondingly, the power weights of the two OAM components of $L=2$ and 4 are both about 43.8%, as shown in Fig. 2(d3). As the l value increases to 3.5, four phase singularities on the x axis and y axis gradually move toward the origin, while the bright fringes on the x axis and the bright spots on the y axis begin to connect together and a quasiring with a larger radius is gradually formed. The power weight of the OAM component of $L=4$ further increases to 84% and that of $L=2$ decreases to 9.3%. Finally, as $l=4$, the PPAV returns to the CAV. In this case, four phase

singularities are completely moved to the origin, a bright ring with a larger radius is obtained, and the power weight of the OAM of $L=4$ is about 100%. To gain an insight into the evolution process of the PPAV, we carefully investigate the properties of PPAVs with TCs increasing from 2 to 4 with an interval of 0.25 in the Supplemental Material [42], when the period number, N , is fixed at 2.

Additionally, we investigate the influence of the period number, N , on the acoustic properties of the proposed PPAVs. In Fig. 3, the first row shows the variation of ψ_{PPAV} of the PPAVs with $l=1.5$ and $N=1$, $l=3$ and $N=2$, $l=4.5$ and $N=3$, and $l=6$ and $N=4$ with azimuthal angle θ . The phase shifts, A , and the phase jumps, B , for four PPAVs are all fixed at 2π and π , respectively. The second row represents the normalized analytical acoustic intensity distributions of the PPAVs with $l=1.5$ and $N=1$ [Figs. 3(b1)], $l=3$ and $N=2$ [Figs. 3(b2)], $l=4.5$ and $N=3$ [Figs. 3(b3)], and $l=6$ and $N=4$ [Figs. 3(b4)] at a plane of $z=7\lambda$, while the corresponding phase profiles are shown in Figs. 3(c1)–3(c4). As seen in Figs. 3(b1) and 3(c1), two phase singularities emerge on the positive and negative y axis, resulting in, respectively, a dark spot (indicated by a white open circles) in the upper part of the pressure-field profile and a low-intensity stripe (indicated by a red-dashed ellipse) along the horizontal direction. These results match well with those of an AV with a fractional TC of 1.5 [8,37]. In this case, the PPAV returns to the AV with a TC of 1.5. It was reported that the AV with a fractional TC could be viewed as the superposition of a series of AVs with integer TCs, each one weighted with the Fourier coefficient [38]. The bottom row in Fig. 3(d1)

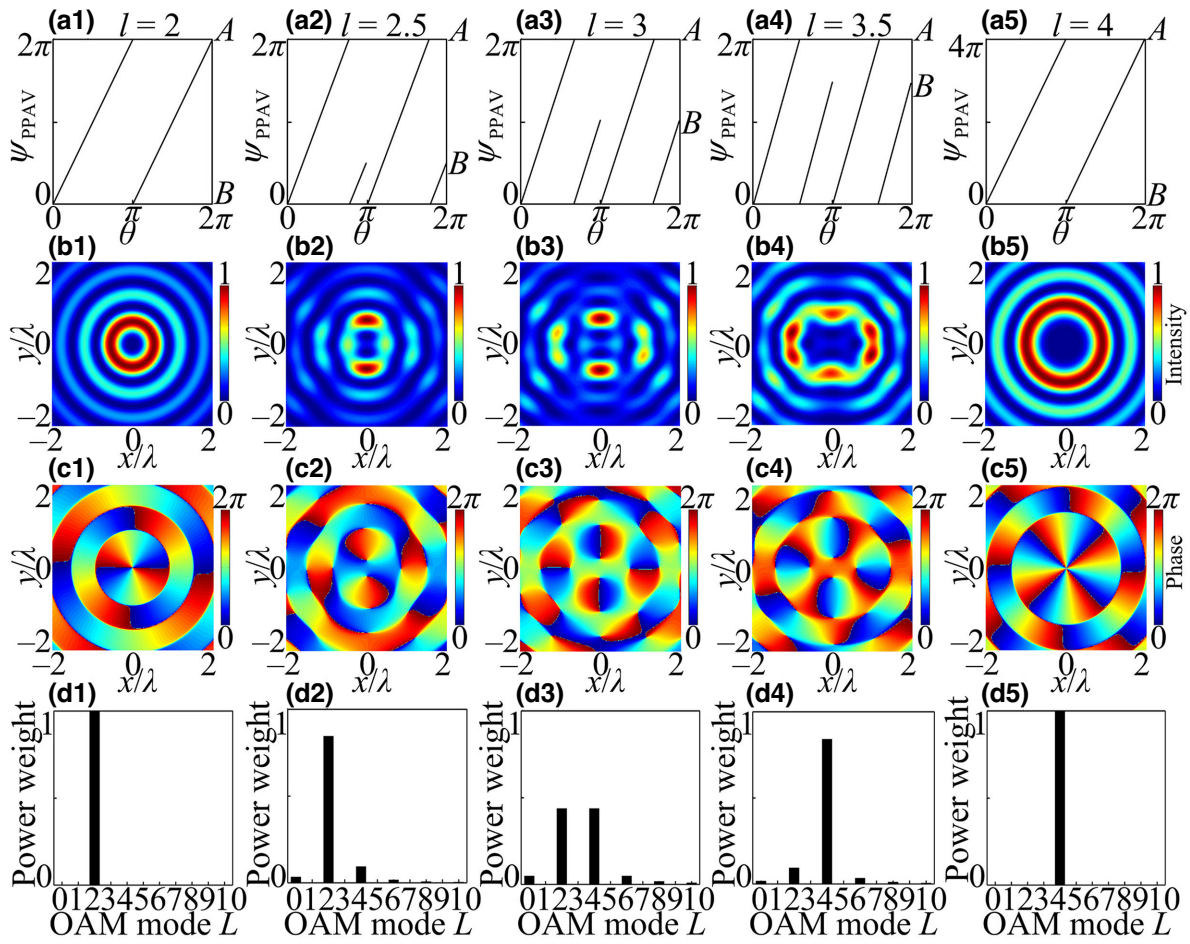


FIG. 2. (a1)–(a5) Dependencies of phase ψ_{PPAV} of the PPAVs with $l=2, 2.5, 3, 3.5,$ and 4 on azimuthal angle θ . Here, period number N is fixed at 2. (b1)–(b5) Normalized analytical acoustic intensity and (c1)–(c5) phase distributions of PPAVs with $l=2, 2.5, 3, 3.5,$ and 4 . Here, the observed plane is $z=7\lambda$. (d1)–(d5) Corresponding OAM spectra of the PPAVs.

shows the OAM spectrum of the PPAV with $l=1.5$ and $N=1$. The power is mainly distributed in two OAM components of $L=1$ and 2, and the power weights of both are about 43.2%. There are some other components with a sample interval of 1, and the power weight of the OAM components of $L=0, 3, 4, 5, 6, 7, 8, 9,$ and 10 are about 4.8%, 4.8%, 1.7%, 0.8%, 0.5%, 0.36%, 0.3%, 0.2%, and 0.15%, respectively.

When $l=3$ and $N=2$, as discussed above, the power weights of the two OAM components of $L=2$ and 4 are both about 43.8%, and the sample interval of the OAM spectrum is 2. For the PPAV with $l=4.5$ and $N=3$, the phase jump, B , of π and the period number of 3 induce the central phase singularity to split into three phase singularities with the same angular interval. Meanwhile, three new phase singularities are formed in the outer part of the phase profile. The power weights of the two OAM components of $L=3$ and 6 are both about 45%, and the sample interval of the OAM components is 3, as shown in Fig. 3(d3). When $l=6$ and $N=4$, as shown in Figs. 3(b4) and 3(c4),

there are four phase singularities that split from the origin, and four phase singularities on the outer part of the phase distribution lead to four dark stripes (indicated by four red-dashed ellipses) on the outer portion of the intensity profile. In Fig. 3(d4), the sample interval of the OAM components is 4, and the power weights of the two OAM components of $L=4$ and 8 are both about 47.4%. Therefore, we further confirm that the sample interval of the components in the OAM spectrum of the PPAV is equal to the period number, N . In the Supplemental Material [42], we also study the acoustic intensity and phase distributions of the PPAVs with the same TC, l , but varying period number, N , and further confirm that the sample interval of the components in the OAM spectrum of the PPAV is equal to the period number, N .

An acoustic artificial-structure plate engraved with 24 circular holes is proposed to achieve the PPAVs, as shown in Fig. 4(a). The AASP is made of stainless steel, and its thickness, d_1 , is fixed at 8 mm ($\sim 5.3\lambda$). The density, longitudinal-wave speed, and shear-wave speed of

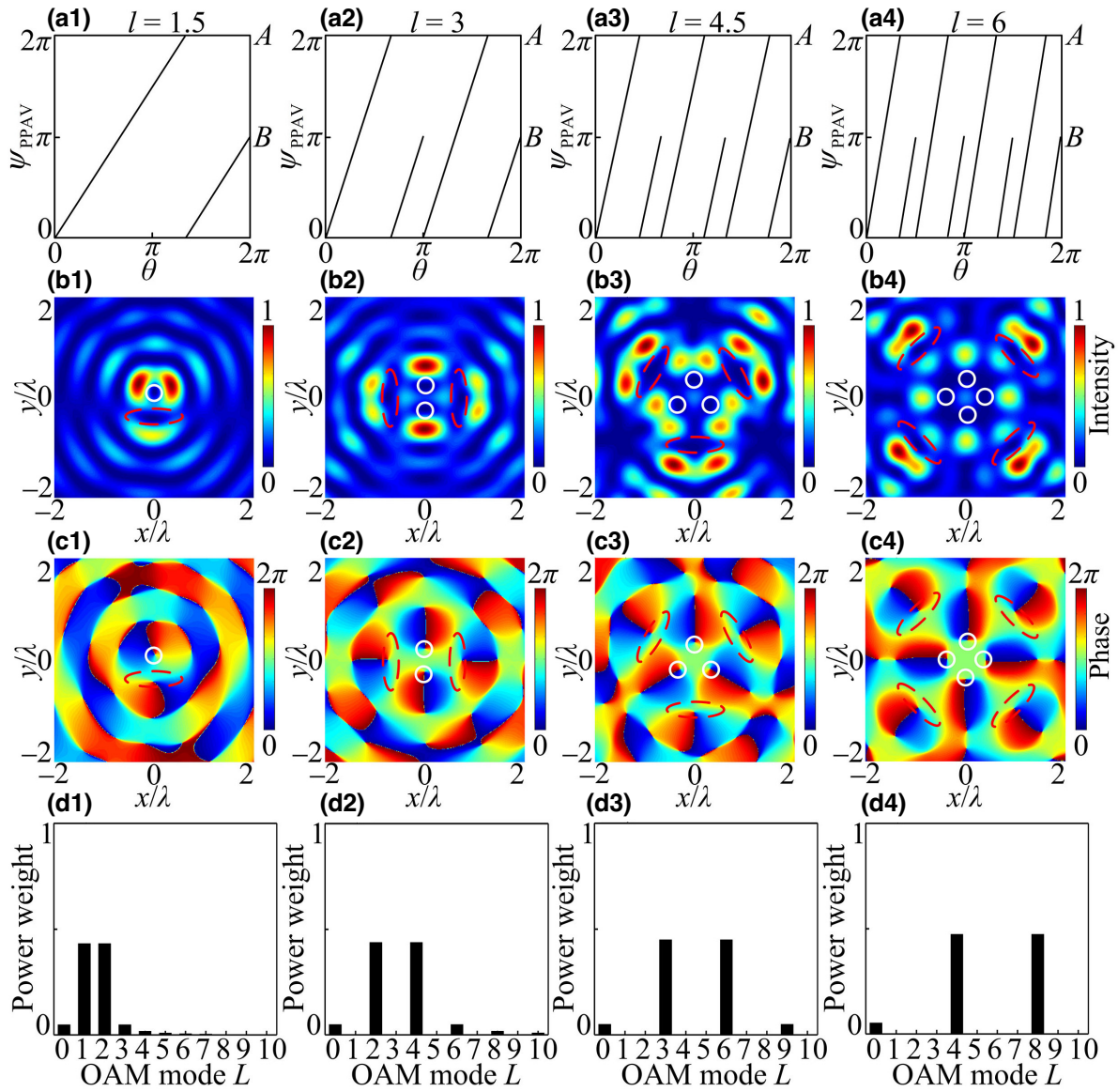


FIG. 3. Variations of phase ψ_{PPAV} of PPAVs with (a1) $l=1.5$ and $N=1$, (a2) $l=3$ and $N=2$, (a3) $l=4.5$ and $N=3$, and (a4) $l=6$ and $N=4$ with θ . (b1)–(b4) Normalized analytical acoustic intensity and (c1)–(c4) phase distributions of PPAVs with $l=1.5$ and $N=1$, $l=3$ and $N=2$, $l=4.5$ and $N=3$, and $l=6$ and $N=4$. Here, the observed plane is $z=7\lambda$. (d1)–(d4) Corresponding OAM spectra of the PPAVs.

stainless steel are 7900 kg m^{-3} , 5240 m s^{-1} , and 2978 m s^{-1} , respectively, and the acoustic impedance is about 28 times that of water [6,34]. Thus, it can be used as an acoustic rigid material in water. As shown in Fig. 4(b), each hole is filled by a resin layer with a height of h (region I), which is connected to a resin base plate with a thickness, d_2 , of λ . The density and acoustic speed of the photosensitive resin are 1120 kg m^{-3} and 2929 m s^{-1} , respectively [1]. The radius of the CH is $w=2.4 \text{ mm}$ ($\sim 1.6\lambda$) and region II is filled with water. Figure 4(c) shows the variations of the transmissivity and transmitted phase shift of the acoustic plane wave through the CH with height h of the resin layer. It is observed that, by changing h from 0 to 8 mm, the

transmitted phase shift can change from 0 to 2π with relatively high transmissivity. For example, when the h values of the resin layer are set as 1.01, 7.67, 4.96, 2.2204, 5.626, 3.03, 3.43, and 6.79 mm, respectively, the corresponding transmitted phase shifts are about 0, $\pi/4$, $\pi/2$, $3\pi/4$, π , $5\pi/4$, $6\pi/4$, and $7\pi/4$. We fabricate an AASP that contains 24 CHs filled with different thicknesses of resin layer to realize the PPAV with $l=3$ and $N=2$.

Figures 4(d) and 4(e) show the simulated normalized acoustic intensity distribution and phase distribution of the transmitted acoustic field through the AASP at a plane of $z=7\lambda$, which are almost in accordance with the analytical results for the PPAV with $l=3$ and $N=2$. In the simulated

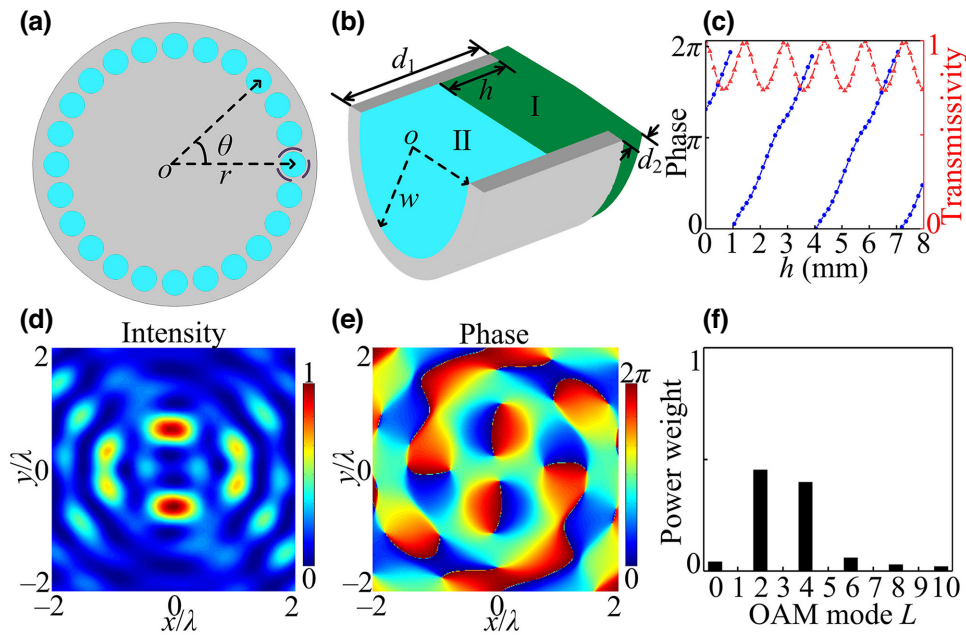


FIG. 4. (a) Schematic diagram of the AASP for generating the PPAV with $l=3$ and $N=2$. (b) Three-dimensional diagram of the CH unit filled with a resin layer. (c) Variations of transmissivity and phase shift of the transmitted acoustic field through one CH unit with thickness h of the filling resin layer. (d) Normalized simulated acoustic intensity distribution, (e) phase distribution, and (f) OAM spectrum of the transmitted acoustic field through the AASP. Here, the observed plane is $z = 7\lambda$.

OAM spectrum shown in Fig. 4(f), the power is still mainly distributed in two OAM components of $L = 2$ ($\sim 45\%$) and 4 ($\sim 40\%$) and the sample interval of the OAM spectrum is 2.

Based on the simulations, we further fabricate an AASP sample to experimentally realize a PPAV. Figure 5(a) shows a photograph of the AASP sample for generating a PPAV with $l=3$ and $N=2$ in water. The AASP substrate engraved with 24 CHs is made of stainless steel using laser-engraving technology and the filling resin layer of each CH is fabricated using three-dimensional printing technology. In the experiment, an ultrasound transducer with a central frequency of 1 MHz is placed on the back of the AASP sample, which is supported by a clamp holder. A needle hydrophone (NH0500, Precision Acoustics) is used to measure the acoustic field, which is fixed on an x - y - z control system. Figures 5(b) and 5(c) represent the normalized measured acoustic intensity and phase distributions of the PPAV, respectively, with $l=3$ and $N=2$ at a plane of $z \approx 7\lambda$. It is observed that there are two bright spots and two dark spots on the y axis and two dark stripes on the x axis in the measured acoustic intensity distributions, while four phase singularities distinctly appear in the measured phase profile. The experimental results match well with the simulated and analytical results. Therefore, the proposed AASP can generate the PPAV experimentally.

Finally, we propose acoustic encoding-decoding communication based on the OAM sample interval of the PPAV, where the OAM sample interval is chosen as an

independent degree of freedom for information encoding-decoding. Here, we introduce the binary code as a reference for encoding-decoding communication, and thus, two PPAVs are used to represent two binary codes of “0” and “1.” In Figs. 6(a) and 6(b), two PPAVs are set as two bases, B_0 and B_1 , corresponding to 0 and 1 in binary representation, respectively. For base B_0 (PPAV with $l=3$ and $N=2$) in Fig. 6(a), the power weights of two OAM

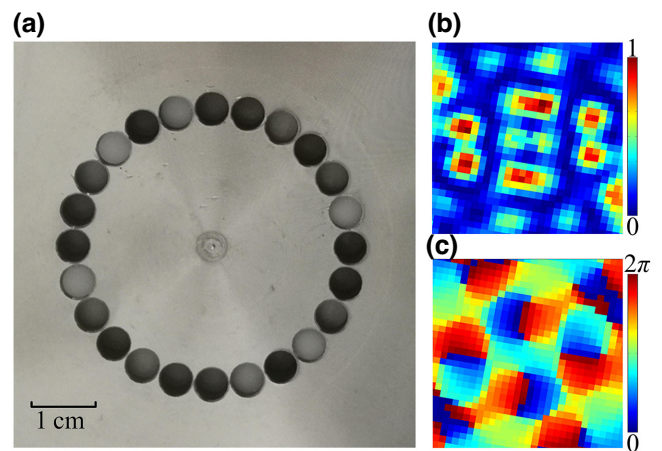


FIG. 5. (a) Photograph of the AASP sample for generating a PPAV with $l=3$ and $N=2$ in water. (b) Normalized measured acoustic intensity and (c) phase distributions of the PPAV with $l=3$ and $N=2$ at a plane of $z \approx 7\lambda$.

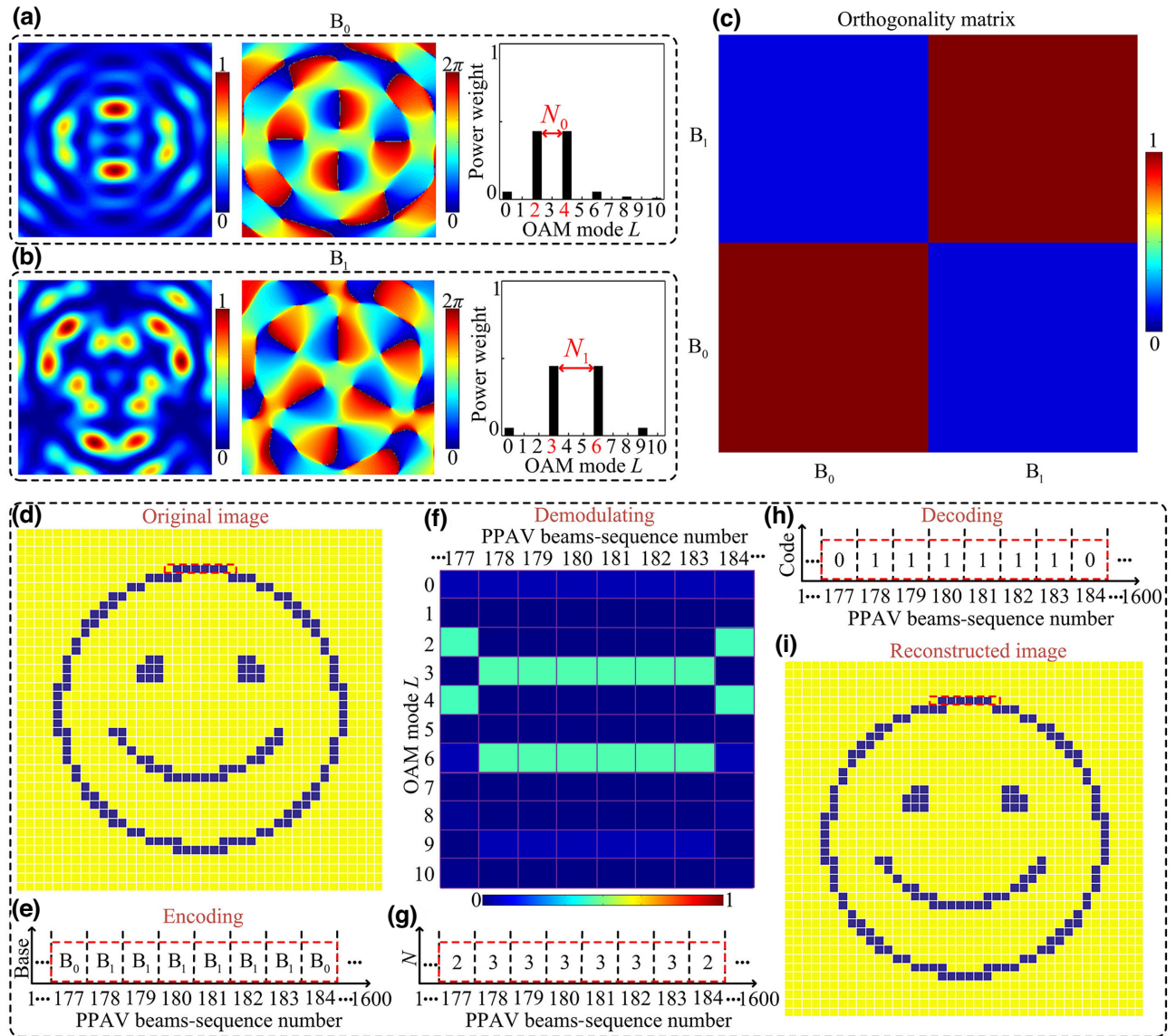


FIG. 6. Scheme for acoustic coded communication based on PPAVs. Normalized analytical acoustic intensity distributions, phase distributions, and OAM spectra of two bases (a) B_0 and (b) B_1 at a plane of $z = 7\lambda$. (c) Orthogonality matrix between B_0 and B_1 . (d) Original image of a smiling face. (e) PPAV beam sequence at the transmitter end. (f) Demodulated OAM spectra of eight PPAVs in the sequence on the receiver side and (g) corresponding OAM sample interval N . (h) Decoded binary data stream and (i) reconstructed image.

components of $L=2$ and 4 account for the largest proportion, and the OAM sample interval N_0 is equal to 2 . The PPAV with $l=4.5$ and $N=3$ is encoded as base B_1 , as shown in Fig. 6(b). The power weights of two OAM components of $L=3$ and 6 account for the largest proportion, and the OAM sample interval N_1 is equal to 3 . Thus, the codes 0 and 1 can be decoded by calculating “ $N-2$.” Figure 6(c) represents the orthogonality matrix between the two bases B_0 and B_1 by means of the inner product between two acoustic pressure distributions [6]. It is found that B_0 and B_1 are orthogonal to each other, and the crosstalk between them is calculated to be less than

about -10.4 dB, which is lower than that in Refs. [4,6]. Therefore, the orthogonal PPAVs can be used in an acoustic communication system. In principle, other orthogonal PPAVs can also be used for encoding-decoding information. If we encode in quaternary, four PPAVs should be encoded as four quaternary codes of “0,” “1,” “2,” and “3.”

In Fig 6(d), a picture of a smiling face discretized into 40×40 pixels is used as the original image. Each pixel can be translated into a binary code of 0 or 1 , according to the “yellow” or “blue” color, respectively. For example, the colors from the 177th pixel to the 184th pixel of the original image are yellow, blue, blue, blue, blue, blue, blue,

and yellow, which are translated into eight binary codes of 0, 1, 1, 1, 1, 1, 1, and 0, respectively. Therefore, they can be encoded as a beam sequence with eight PPAVs of “ $B_0B_1B_1B_1B_1B_1B_1B_0$ ” at the transmitter end, as shown in Fig. 6(e). Figure 6(f) shows the demodulated OAM spectra of eight PPAVs in the sequence on the receiver side and the corresponding OAM sample interval N is “23333332” [Fig. 6(g)]. Thus, the obtained decoded binary data stream is “01111110,” according to $N-2$ [Fig. 6(h)]. Finally, the transmitted image is reconstructed, as shown in Fig. 6(i). The OAM sample interval of the PPAV can be chosen as an independent degree of freedom for acoustic encoding-decoding communication with less crosstalk. Moreover, it has been reported that multipath systems are helpful for delivering high capacity in free space [39,40]. To further demonstrate the potential of the OAM sample interval of the PPAV in acoustic communication, we additionally develop a multipath parallel communication system in the Supplemental Material [42].

IV. CONCLUSION

We proposed a PPAV with a comblike OAM spectrum, and the sample interval of the OAM spectrum of the PPAV could be adjusted by changing the period number of the azimuthal phase. The dynamic variations of the acoustic properties of the PPAVs with increasing TC were clarified carefully. The sample interval of the components in the OAM spectrum of the PPAV was further confirmed to be the same as the period number, N . Moreover, an AASP engraved with 24 filled CHs was designed to achieve the PPAVs in water. As an ultrasonic plane wave illuminated the AASP, the transmitted phase shift of the CH unit could be flexibly and efficiently manipulated by changing the height of the resin layer filling each hole unit; hence, the PPAV with an arbitrary TC could be generated by the AASP. We fabricated an AASP sample and experimentally confirmed the generation of the PPAV by the well-designed AASP. Finally, we confirmed that the OAM sample interval of the PPAV could be chosen as an independent degree of freedom for acoustic encoding-decoding communication. Indeed, the inhomogeneous medium in the real underwater environment led to the reflection and refraction of acoustic waves due to the change in density [41]. Zou *et al.* [19] experimentally placed a vortex source below the water surface, and the source was oriented upward toward the water-air boundary at an angle of 45° . It was found that the incident and reflected phase patterns were reversed. The communication performance should also be characterized by the data-transmission rate, spectrum efficiency, bit-error rate, etc. These are necessary for exploring the practical applications of AVs in a real underwater environment. Therefore, more work should be put into our future experimental investigations on the

transmission of PPAVs in inhomogeneous media and the effectiveness of communication.

ACKNOWLEDGMENTS

This work was supported by the National Natural Science Foundation of China (Grants No. 12174197, No. 12374439, and No. 12027808) and the Postgraduate Research & Practice Innovation Program of Jiangsu Province (Grant No. KYCX22_1537).

- [1] Q. X. Zhou, J. Zhang, X. M. Ren, Z. Xu, and X. J. Liu, Acoustic trapping of particles using a Chinese taiji lens, *Ultrasonics* **110**, 106262 (2021).
- [2] Z. Y. Sun, Y. Shi, X. C. Sun, H. Jia, Z. K. Jin, K. Deng, and J. Yang, Underwater acoustic multiplexing communication by pentamode metasurface, *J. Phys. D: Appl. Phys.* **54**, 205303 (2021).
- [3] Z. Y. Hong, J. Zhang, and B. W. Drinkwater, On the radiation force fields of fractional-order acoustic vortices, *Europhys. Lett.* **110**, 14002 (2015).
- [4] C. Z. Shi, M. Dubois, Y. Wang, and X. Zhang, High-speed acoustic communication by multiplexing orbital angular momentum, *Proc. Natl. Acad. Sci. U. S. A.* **114**, 7250 (2017).
- [5] X. Jiang, B. Liang, J. C. Cheng, and C. W. Qiu, Twisted acoustics: Metasurface-enabled multiplexing and demultiplexing, *Adv. Mater.* **30**, 1800257 (2018).
- [6] X. R. Li, Y. R. Jia, Y. C. Luo, J. Yao, and D. J. Wu, Coupled focused acoustic vortices generated by degenerated artificial plates for acoustic coded communication, *Adv. Mater. Technol.* **7**, 2200102 (2022).
- [7] X. R. Li, Y. R. Jia, Y. C. Luo, J. Yao, and D. J. Wu, Mixed focused-acoustic-vortices generated by an artificial structure plate engraved with discrete rectangular holes, *Appl. Phys. Lett.* **118**, 043503 (2021).
- [8] Y. C. Luo, Y. R. Jia, J. Yao, D. J. Wu, and X. J. Liu, Enhanced fractional acoustic vortices by an annulus acoustic metasurface with multi-layered rings, *Adv. Mater. Technol.* **5**, 2000356 (2020).
- [9] S. W. Fan, Y. F. Wang, L. Y. Cao, Y. F. Zhu, A. Chen, B. Vincent, B. Assouar, and Y. S. Wang, Acoustic vortices with high-order orbital angular momentum by a continuously tunable metasurface, *Appl. Phys. Lett.* **116**, 163504 (2020).
- [10] Q. Feng, X. D. Kong, M. M. Shan, Y. F. Lin, L. Li, and T. J. Cui, Multi-Orbital-Angular-Momentum-Mode Vortex Wave Multiplexing and Demultiplexing with Shared-Aperture Reflective Metasurfaces, *Phys. Rev. Appl.* **17**, 034017 (2022).
- [11] J. J. Jin, X. Li, M. B. Pu, Y. H. Guo, P. Gao, M. F. Xu, Z. J. Zhang, and X. G. Luo, Angular-multiplexed multi-channel optical vortex arrays generators based on geometric metasurface, *iScience* **24**, 102107 (2021).
- [12] L. J. Yang, S. Sun, and W. E. I. Sha, Manipulation of orbital angular momentum spectrum using shape-tailored metasurfaces, *Adv. Opt. Mater.* **9**, 2001711 (2021).

- [13] V. V. Kotlyar and A. A. Kovalev, Optical vortex beams with a symmetric and almost symmetric OAM spectrum, *J. Opt. Soc. Am. A*, **38**, 1276 (2021).
- [14] H. P. Zhou, J. J. Li, K. Guo, and Z. Y. Guo, Generation of acoustic vortex beams with designed Fermat's spiral diffraction grating, *J. Acoust. Soc. Am.* **146**, 4237 (2019).
- [15] M. P. J. Lavery, Vortex instability in turbulent free-space propagation, *New J. Phys.* **20**, 043023 (2018).
- [16] M. Li, Orbital-angular-momentum multiplexing optical wireless communications with adaptive modes adjustment in internet-of-things networks, *IEEE Internet Things J.* **6**, 6134 (2019).
- [17] K. Wu, J. J. Liu, Y. J. Ding, W. Wang, B. Liang, and J. C. Cheng, Metamaterial-based real-time communication with high information density by multipath twisting of acoustic wave, *Nat. Commun.* **13**, 5171 (2022).
- [18] J. J. Liu, Y. J. Ding, K. Wu, B. Liang, and J. C. Cheng, Compact acoustic monolayered metadecoder for efficient and flexible orbital angular momentum demultiplexing, *Appl. Phys. Lett.* **119**, 213502 (2021).
- [19] Z. G. Zou, R. Lirette, and L. K. Zhang, Orbital Angular Momentum Reversal and Asymmetry in Acoustic Vortex Beam Reflection, *Phys. Rev. Lett.* **125**, 074301 (2020).
- [20] M. Li, M. Cvijetic, Y. Takashima, and Z. Yu, Evaluation of channel capacities of OAM based FSO link with real-time wavefront correction by adaptive optics, *Opt. Express* **22**, 31337 (2014).
- [21] M. Li, Z. Yu, and M. Cvijetic, Influence of atmospheric turbulence on OAM-based FSO system with use of realistic link model, *Opt. Commun.* **364**, 50 (2016).
- [22] Y. Yan, G. D. Xie, M. P. J. Lavery, H. Huang, N. Ahmed, C. J. Bao, Y. X. Ren, Y. W. Cao, L. Li, Z. Zhao, A. F. Molisch, M. Tur, M. J. Padgett, and A. E. Willner, High-capacity millimetre-wave communications with orbital angular momentum multiplexing, *Nat. Commun.* **5**, 4876 (2014).
- [23] M. Zahidy, Y. X. Liu, D. Cozzolino, Y. H. Ding, T. Morioka, L. K. Oxenlowe, and D. Bacco, Photonic integrated chip enabling orbital angular momentum multiplexing for quantum communication, *Nanophotonics* **11**, 821 (2021).
- [24] M. Barbuto, M. A. Miri, A. Alù, F. Bilotti, and A. Toscano, Exploiting the topological robustness of composite vortices in radiation systems, *Prog. Electromag. Res.* **162**, 39 (2018).
- [25] Y. J. Yang, Q. Zhao, L. L. Liu, Y. D. Liu, C. Rosales-Guzmán, and C. W. Qiu, Manipulation of Orbital-Angular-Momentum Spectrum Using Pinhole Plates, *Phys. Rev. Appl.* **12**, 064007 (2019).
- [26] Z. Qiao, Z. Y. Wan, G. Q. Xie, J. Wang, L. J. Qian, and D. Y. Fan, Multi-vortex laser enabling spatial and temporal encoding, *Photonix* **1**, 13 (2020).
- [27] H. X. Ma, X. Z. Li, H. Zhong, J. Tang, H. H. Li, M. M. Tang, J. G. Wang, and Y. J. Cai, Optical vortex shaping via a phase jump factor, *Opt. Lett.* **44**, 1379 (2019).
- [28] J. T. Hu, Y. P. Tai, L. H. Zhu, Z. X. Long, M. M. Tang, H. H. Li, X. Z. Li, and Y. J. Cai, Optical vortex with multifractional orders, *Appl. Phys. Lett.* **116**, 201107 (2020).
- [29] H. Q. Liu, C. X. Teng, H. Y. Yang, H. G. Deng, R. H. Xu, S. J. Deng, M. Chen, and L. B. Yuan, Proposed phase plate for superimposed orbital angular momentum state generation, *Opt. Express* **26**, 14792 (2018).
- [30] Z. Sun, H. Z. Guo, and I. F. Akyildiz, High-data-rate long-range underwater communications via acoustic reconfigurable intelligent surfaces, *IEEE Commun. Mag.* **60**, 96 (2022).
- [31] P. Q. Li, Z. L. Li, W. Zhou, S. W. Wang, L. Meng, Y. G. Peng, Z. Chen, H. R. Zheng, and X. F. Zhu, Generating multistructured ultrasound via bioinspired metaskin patterning for low-threshold and contactless control of living organisms, *Adv. Funct. Mater.* **32**, 2203109 (2022).
- [32] L. Tong, Z. Xiong, Y. X. Shen, Y. G. Peng, X. Y. Huang, L. Ye, M. Tang, F. Y. Cai, H. R. Zheng, J. B. Xu, G. J. Cheng, and X. F. Zhu, An acoustic meta-skin insulator, *Adv. Mater.* **32**, 2002251 (2020).
- [33] Y. X. Shen, Y. G. Peng, F. Y. Cai, K. Huang, D. G. Zhao, C. W. Qiu, H. R. Zheng, and X. F. Zhu, Ultrasonic superoscillation wave-packets with an acoustic meta-lens, *Nat. Commun.* **10**, 3411 (2019).
- [34] X. Jiang, J. J. Zhao, S. L. Liu, B. Liang, A. Y. Zou, J. Yang, C. W. Qiu, and J. C. Cheng, Broadband and stable acoustic vortex emitter with multi-arm coiling slits, *Appl. Phys. Lett.* **108**, 203501 (2016).
- [35] X. M. Ren, Q. X. Zhou, Z. Xu, and X. J. Liu, Particle Trapping in Arbitrary Trajectories Using First-Order Bessel-Like Acoustic Beams, *Phys. Rev. Appl.* **15**, 054041 (2021).
- [36] Y. J. Yang, G. Thirunavukkarasu, M. Babiker, and J. Yuan, Orbital-Angular-Momentum Mode Selection by Rotationally Symmetric Superposition of Chiral States with Application to Electron Vortex Beams, *Phys. Rev. Lett.* **119**, 094802 (2017).
- [37] Y. R. Jia, W. Q. Ji, D. J. Wu, and X. J. Liu, Metasurface-enabled airborne fractional acoustic vortex emitter, *Appl. Phys. Lett.* **113**, 173502 (2018).
- [38] N. Zhang, J. A. Davis, I. Moreno, J. Lin, K. J. Moh, D. M. Cottrell, and X. C. Yuan, Analysis of fractional vortex beams using a vortex grating spectrum analyzer, *Appl. Opt.* **49**, 2456 (2010).
- [39] Y. X. Ren, Z. Wang, G. D. Xie, L. Li, Y. W. Cao, C. Liu, P. C. Liao, Y. Yan, N. Ahmed, Z. Zhao, A. Willner, N. Ashrafi, S. Ashrafi, R. D. Linquist, R. Bock, M. Tur, A. F. Molisch, and A. E. Willner, Free-space optical communications using orbital-angular-momentum multiplexing combined with MIMO-based spatial multiplexing, *Opt. Lett.* **40**, 4210 (2015).
- [40] Q. B. Zhu, T. Jiang, D. M. Qu, D. Chen, and N. R. Zhou, Radio vortex-multiple-input multiple-output communication systems with high capacity, *IEEE Access* **3**, 2456 (2015).
- [41] H. Kaushal and G. Kaddoum, Underwater optical wireless communication, *IEEE Access* **4**, 1518 (2016).
- [42] See the Supplemental Material at <http://link.aps.org/supplemental/10.1103/PhysRevApplied.20.034008> for the propagation properties of the PPAV, the acoustic intensity and phase distributions produced by the first and second phase periods of the PPAV with $l=3$ and $N=2$, a detailed evolution process of the PPAV, PPAVs with same TC l but varying period number N , and a multipath parallel acoustic encoding-decoding communication system for sending letters.